Effect of precipitation mineralization reactions on convective dissolution of CO$_2$: An experimental study

C. Thomas, S. Dehaeck ⓘ, and A. De Wit ⓘ[*]

Université Libre de Bruxelles (ULB), Nonlinear Physical Chemistry Unit, CP231, 1050 Brussels, Belgium

To analyze the influence of a precipitation mineralization reaction between dissolved CO$_2$ and calcium ions on the convective transfer of CO$_2$ toward an aqueous phase, the convective dissolution of CO$_2$ into aqueous solutions of calcium hydroxyde [Ca(OH)$_2$] and calcium chloride (CaCl$_2$) of various concentrations is studied experimentally. We show that different precipitation patterns develop in the aqueous solution depending on the nature and concentration of the reactant in the host phase. In the case of Ca(OH)$_2$, precipitation coupled to convection leads to vigorous convective mixing in the host phase and sedimentation of solid particles of calcium carbonate (CaCO$_3$) down to the bulk of the reservoir. Conversely, dissolution of CO$_2$ in buffered CaCl$_2$ solutions leads to a stabilization of the buoyancy-driven convection due to a decrease in density and the adherence of the precipitate to the cell walls.

I. INTRODUCTION

In order to decrease the amount of greenhouse gases in the atmosphere and reduce global warming, carbon capture and sequestration (CCS), whereby CO$_2$ is injected into geological formations, is currently being investigated on various pilot sites [1,2]. In parallel, fundamental research is being performed in order to more accurately predict the storage capacity of the different sequestration locations [3,4]. In this regard, one topic of active research is the study of the convective instabilities arising upon dissolution of CO$_2$ in host saline aquifers. Indeed, as dissolution progresses, the local density below the CO$_2$/brine interface is increasing, which eventually leads to the development of denser fingers sinking down in the brine [5–8]. This convective motion leads to a faster mixing and uptake of CO$_2$ in the brine and hence is a favorable process for the efficiency and safety of sequestration. Recently, it has been shown both experimentally [7] and theoretically [9] that the properties of the convective fingers depend on the salinity of the host solution, with stabilization of convection as salinity increases. In realistic geological conditions, chemical reactions can also affect the convective dissolution of CO$_2$ [4,10–15]. As an example, alkaline metal ions can be found in large concentrations in basalts, in which CCS has been tested [1]. Those basic rocks, widely present on Earth, are generally rich in Ca^{2+} ions. Dissolution of such rocks due to the injection of acidic CO$_2$ in deep aquifers will lead to "mineral trapping" or "mineral carbonation," where the CO$_2$ is converted by reaction with Ca^{2+} into stable carbonate minerals such as calcite (CaCO$_3$). This mineralization process is expected to increase storage capacity and reduce the risk of leakage, and is therefore particularly interesting for an efficient long-term storage of CO$_2$ [1,13,14]. However, these dissolution-precipitation reactions might irreversibly modify the physical characteristics of the reservoir, such as its porosity or permeability [16–18], which could have a dramatical impact on the safety of the storage process. Hence, much research has been devoted to the analysis of the

---

[*]adewit@ulb.ac.be

impact of precipitation and/or dissolution processes upon CO_2 injection in reactive porous media on the local permeability and porosity of the reservoir [18–24].

In addition, geochemical reactions can also affect the buoyancy-driven convection promoting the transport of CO_2 in host aquifers once it has dissolved in them. Precipitation reactions can delay and hinder convective dissolution as the consumption of CO_2 to generate a solid product fixed to the porous matrix decreases the concentration of the dissolved CO_2, thereby decreasing the unstable density gradient at the origin of the instability [3,4,11]. This is indeed the case if CO_2 fixes itself by precipitation to the porous matrix and does not contribute to changing the density of the solution any longer. However, some precipitate may remain in solution and can be entrained by the convective flows, an effect that has received less attention so far.
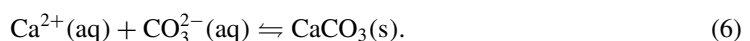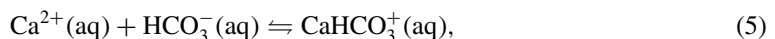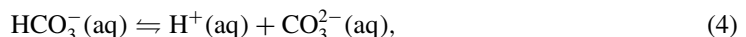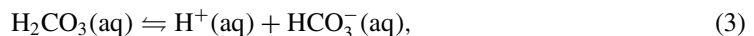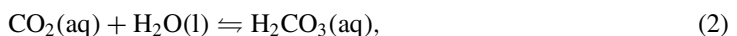
In the context of such flow-driven precipitation, patterns of solid calcium carbonate, $CaCO_3$, have been obtained experimentally upon radial injection of a solution of carbonate (CO_3^{2-}) into a solution of calcium ions (Ca^{2+}) in a horizontal Hele-Shaw cell [15,25,26]. In these experiments, Schuszter *et al.* have demonstrated that changes in the concentration of reactants or in the injection rate can have substantial effects on the spatial distribution of the precipitate as well as on the amount of $CaCO_3$ produced upon reaction. In some cases, precipitation-driven fingering is observed related to local changes in permeability [15,27]. To the best of our knowledge, coupling between precipitation mineralization reactions and buoyancy-driven convection occurring in vertical setups, however, has not been addressed yet.

In this context, we analyze here experimentally the impact of a precipitation reaction between carbonate and calcium ions upon CO_2 convective dissolution in aqueous solutions of Ca^{2+} ions in a vertical Hele-Shaw cell. We do not consider here the reaction of dissolved CO_2 with the porous rock but rather focus on reactions occurring within the aqueous phase. To study the precipitation process in various reactive environments, two different reactants are used to release Ca^{2+} ions in the reactive solution. First, CO_2 is dissolved in solutions of calcium hydroxide $Ca(OH)_2$ of various concentrations. This strong base reactant is a model system for some ultrabasic rocks, the dissolution of which can lead to the mobilization of Ca^{2+} and OH^- in the formation water, sometimes yielding pH exceeding 10 [14]. Second, we study the dissolution of CO_2 in solutions of $CaCl_2$. In this case, a buffer is used to reproduce the reported buffering capacity of reservoirs [1,14,19,28,29] and stabilize the pH of the solution. We arbitrarily choose here to work with the borax pH buffer which maintains the pH around 9, which is often considered in experimental studies [19,29]. We show that, depending on the reaction conditions in the host phase, precipitation reactions can have different impacts on convective dissolution.

II. EXPERIMENTAL SETTINGS

A. Mineralization reaction

When CO_2 dissolves into salt water, it can react with metal cations dissolved in the brine, such as calcium ions Ca^{2+}. The following reaction sequence then takes place in the aqueous phase:

$$CO_2(g) \rightleftharpoons CO_2(aq), \tag{1}$$

$$CO_2(aq) + H_2O(l) \rightleftharpoons H_2CO_3(aq), \tag{2}$$

$$H_2CO_3(aq) \rightleftharpoons H^+(aq) + HCO_3^-(aq), \tag{3}$$

$$HCO_3^-(aq) \rightleftharpoons H^+(aq) + CO_3^{2-}(aq), \tag{4}$$

$$Ca^{2+}(aq) + HCO_3^-(aq) \rightleftharpoons CaHCO_3^+(aq), \tag{5}$$

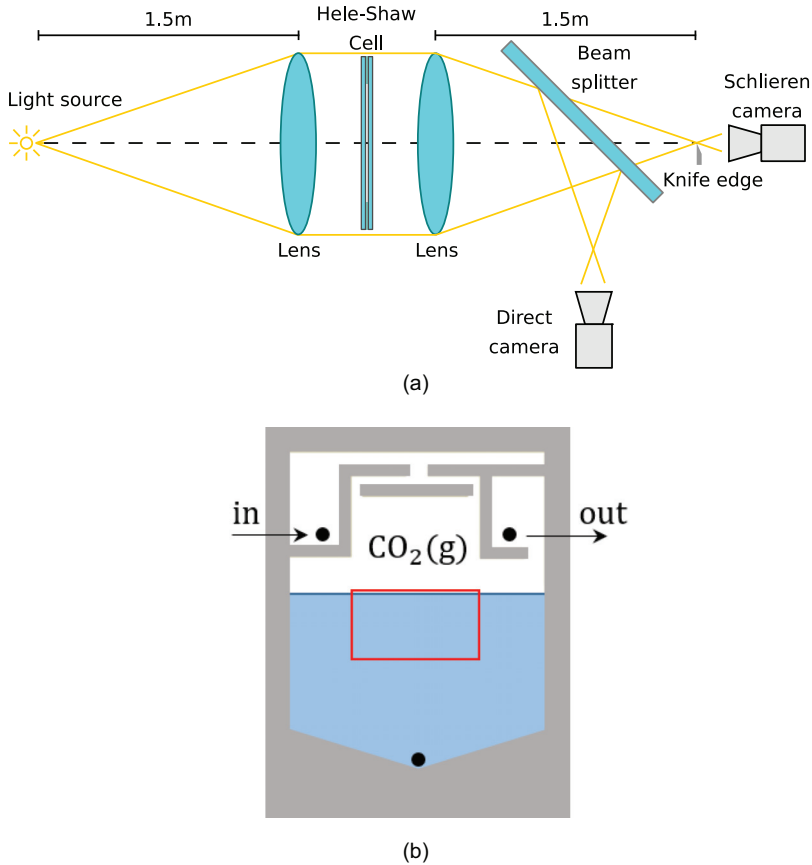$$Ca^{2+}(aq) + CO_3^{2-}(aq) \rightleftharpoons CaCO_3(s). \tag{6}$$

FIG. 1. (a) Schematic of the experimental setup including Schlieren and direct visualization. (b) Design of the spacer and sketch of the two-layer stratification of CO_2 and aqueous reactive solution in the Hele-Shaw cell. The red rectangle shows the zone followed in the study of the convective dynamics.

Equation (6) corresponds to the precipitation reaction of carbonate and calcium ions into solid calcium carbonate. This is one of the key mineralization reactions trapping the CO_2 as solid carbonates in the reservoir for a long period of time. The reverse reaction, i.e., the dissolution of calcium carbonate, is also possible depending on the conditions under which reactions take place (e.g., pH, temperature, pressure). For example, calcium carbonate only forms in solutions where the pH exceeds 5.14 [30].

B. Experimental setup

Experiments are performed in a vertical Hele-Shaw cell made of two glass plates (210 × 260 mm) separated by a gap width of 1 mm. This gap width is set by a silicon rubber spacer designed for a homogeneous injection of CO_2 above the aqueous interface [cf. Fig. 1(b)]. One of the glass plates contains three connectors (quick push-in connectors, Elneo pneumatics, Belgium) in which PFA tubes (perfluoroalkoxy tubes, 1/8-in. outer diameter, 0.030-in. inner diameter, Swagelok, Belgium) are inserted to allow the injection of gases and liquids into the cell. The cell is partially filled with aqueous solutions through the inlet at the bottom of the cell. The two upper inlets are used to let gases (N_2 or CO_2) flow in and out of the cell.

Three visualisation and measurement techniques are used to analyze the dissolution dynamics. The lens-type Schlieren system shown in Fig. 1(a) was already described in Ref. [7]. The lenses used are achromats with focal lengths of 1.5 m and 15 cm diameter. The camera is a 12-bit monochrome camera from Allied Vision Technologies. With a 200-mm micro-Nikkor objective, a central 8.8×4.7 cm field of view is obtained. To increase the sensitivity of the Schlieren system, the cutoff by the knife edge was increased, as well as the exposure time [31]. The main postprocessing steps consisted in the substraction of a reference image taken before the injection of CO_2 and the removal of mean offsets coming from residual, but global, perturbations (vibrations, air currents, etc.).

While the Schlieren system visualizes refractive index gradients as variations in grayscale, it makes such variations indistinguishable from differences in opacity (such as those coming from solid particle formations). Therefore, to track precipitate formation, a direct visualization system was also added by placing a beam splitter in front of the knife edge [Fig. 1(a)]. Note that very strong refractive index gradients could nevertheless still lead to obscuration without the presence of particles.

A third type of visualization, performed for a limited set of experiments, was based on the use of color indicators. Here, pH changes are visualized by addition of a universal color indicator, which gradually changes color from blue or purple in a basic environment to yellow as the pH decreases. For this purpose, the cell is placed in front of a light table (Lightpad) and a Nikon camera directly captures the pH changes at regular time intervals. Even though color indicators have been shown previously to be not the best method to track convective motions [32,33], they are used here to follow different reactive zones depending on their local pH values.

The general protocol for our experiments is the following. First, gaseous N_2 is continuously fed into the cell at a rate of a few hundreds of milliliters per minute. Then, 18 ml of an aqueous solution of reactants is injected from below up to a height of 10 cm. When this injection is completed and a sufficiently flat interface is obtained, the flow of N_2 is replaced with CO_2, injected at the same flow rate. The initial time $t = 0$ s corresponds to the time at which N_2 is replaced by CO_2. Gaseous CO_2 starts to invade the cell a few seconds after the beginning of experiment. Note that both gases pass through a humidifier before entering into the cell to saturate the gases in water. As reported in Ref. [7], in the absence of such a humidifier, the evaporation of water can lead to solutal or thermal instabilities, which are not linked to the dissolution of CO_2 in the water.

C. Calcium hydroxide solutions

Because of the low solubility of calcium hydroxide, concentrated solutions of $Ca(OH)_2$ are challenging to prepare. Moreover, they are also very reactive and the CO_2 present in the ambient air dissolves massively in it and subsequently precipitates in the form of $CaCO_3$. As a consequence, the solution progressively gets cloudy over time. For our experiments, all solutions were prepared from the same stock solution as follows. A large amount (>3 g) of calcium hydroxide (74.09 g/mol, ACS, Reag. Ph. Eur. for analysis, Merck, VWR, Belgium) is poured in a flask containing 1 L of distilled water. As the theoretical solubility of $Ca(OH)_2$ is 1.7 g/L, the resulting solution is oversaturated. Gaseous N_2 is injected inside the flask to remove atmospheric CO_2 before closing it. The solution is next constantly stirred for a period of approximately 6 h. Then, the flask is stored in a quiet place for 2 days. After this time, most of the remaining solid particles [$Ca(OH)_2(s)$ or $CaCO_3(s)$] have sedimented, leaving an upper layer of a clear saturated solution of $Ca(OH)_2$, which is collected to prepare the other solutions. Less concentrated solutions of $Ca(OH)_2$ are obtained from 50%, 10%, 5%, and 1% dilution with distilled water of this stock solution.

The concentration of calcium hydroxide in the saturated stock solution can be estimated thanks to the solubility product K_s of the dissociation reaction. As $K_s = 4.68 \times 10^{-6}$ M^3, the solubility S of $Ca(OH)_2$ is estimated to be close to 10^{-2} M. Concentrations of the 50%, 10%, 5%, and 1% diluted solutions are consequently 5×10^{-3}, 10^{-3}, 5×10^{-4}, and 10^{-4} M. As a comparison, for $CaCO_3$, K_s is equal to 4.96×10^{-9} M^2, leading to a solubility $S = 7.04 \times 10^{-5}$ M. The pH and densities of $Ca(OH)_2$ solutions are given in Table I. We note that in this case the error on $Ca(OH)_2$

TABLE I. pH and density ρ of $Ca(OH)_2$ and $CaCl_2$ solutions. The temperature T at which the density measurement was performed is given in the last column. The concentration of borax is 0.0125 M.

Concentration	pH	ρ (g/cm^3)	T (°C)
$Ca(OH)_2$			
0 M (water)	7.00	0.9985	20.1
10^{-4} M	7.00	0.9983	20.7
5×10^{-4} M	11.20	0.9983	20.6
10^{-3} M	11.85	0.9987	19.9
5×10^{-3} M	12.61	0.9991	21.4
10^{-2} M	12.90	1.0000	21.4
$CaCl_2$			
0 M (borax)	9.45	1.0010	20.1
0.010 M	9.37	1.0016	20.8
0.025 M	9.26	1.0030	20.6
0.050 M	9.18	1.0053	20.6
0.075 M	9.07	1.0075	20.6
0.100 M	9.00	1.0097	20.6

concentrations is difficult to determine. Measured viscosities were found to be similar to water viscosity.

D. Calcium chloride solutions

Calcium chloride is much more soluble in water (solubility $S = 977.0$ g/l $= 6.6$ M) than $Ca(OH)_2$. $CaCl_2$ solutions are here buffered at pH 9 using borax to mimic the natural buffer capacity of basic rock reservoirs. As the convective dynamics might be affected by the presence of borax in the solution, we also performed a few experiments in glycine solutions, another pH buffer, which is a simple amino acid ($C_2H_5NO_2$) [34] commonly used in biochemistry.

Borax solutions of concentration 0.0125 M are prepared by dissolving sodium tetraborate decahydrate (381.37 g/mol, $Na_2B_4O_7 \cdot 10H_2O$, ACS reagent, reag. ISO, buffer substance, $\geqslant 99.5\%$, Fluka, Honeywell Chemicals, VWR, Belgium) into deionised water. Then, solutions of $CaCl_2$ (147.01 g/mol, calcium chloride dihydrate, reagent plus, Honeywell Chemicals, VWR, Belgium) are prepared using the borax buffer solution as a solvent. Solutions of glycine 0.0125 M are prepared by dilution of liquid 0.6 M glycine (Sigma-Aldrich, Belgium) with distilled water, which are then used as solvents to prepare $CaCl_2$ solutions.

We choose to work with a low concentration of borax in order to interfere as little as possible with the convective dynamics. We note that if the concentration of borax is larger than 0.0125 M, we observe the formation of a white precipitate in the flask when $CaCl_2$ is added to the solution. On the other hand, as $CaCl_2$ is slightly acidic in water, the dissolution of this salt lowers the pH of the solution. This is why we work with a maximum concentration of $CaCl_2$ of 0.100 M. Larger concentrations of $CaCl_2$ would weaken the buffering capacity of borax before the experiment. Moreover, this concentration corresponds to typical calcium concentrations measured by Kharaka *et al.* in various geological storage places [35]. The properties of $CaCl_2$ solutions are summarized in Table I.

III. CONVECTIVE DISSOLUTION of CO_2 in solutions of $Ca(OH)_2$

A. Phenomenology

An overview of the temporal development of convection generated by the dissolution of CO_2 in solutions of $Ca(OH)_2$ in the range of concentration 10^{-4} to 10^{-2} M is displayed in Fig. 2 (see also
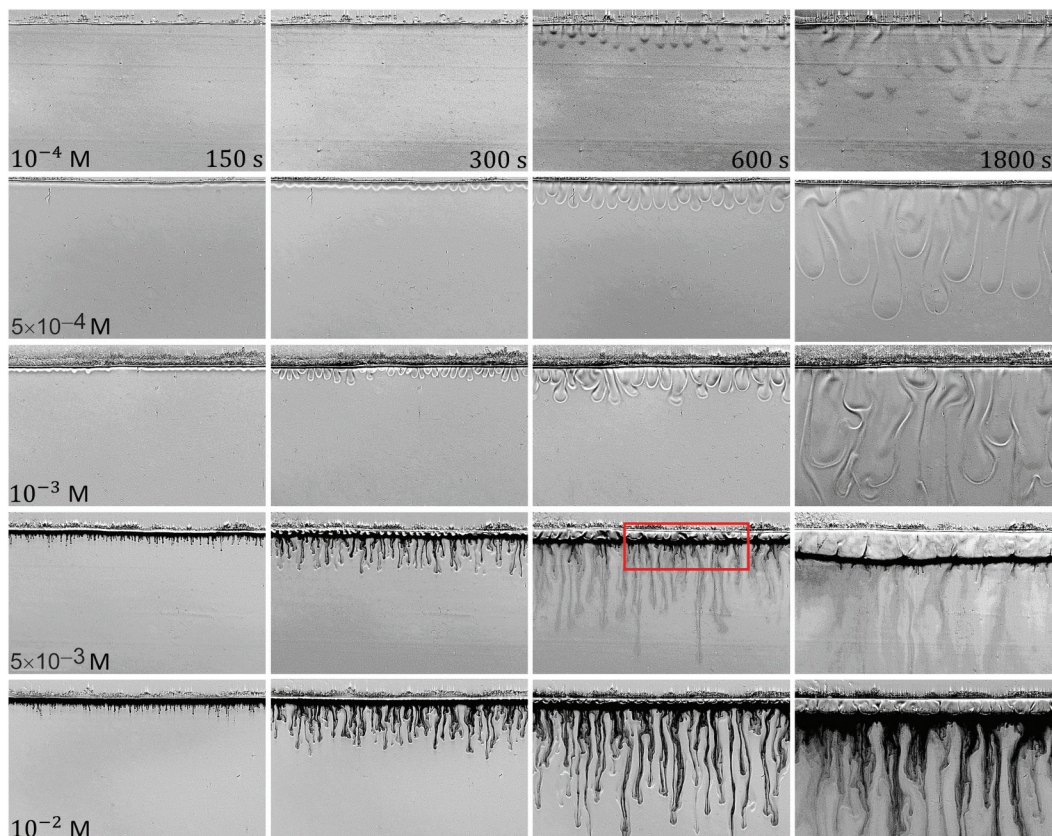
FIG. 2. Schlieren images of the temporal development of the convective instability generated by the dissolution of gaseous CO_2 in $Ca(OH)_2$ solutions of increasing concentration from top to bottom at $t = 150$, 300, 600, and 1800 s from left to right. The field of view is 8.8×5.5 cm. An enlargement of the red rectangle of the image at $t = 600$ s of the solution at 5×10^{-3} M is provided in Fig. 3.

the videos provided in the Supplemental Material [36]). At early times, the dissolution of CO_2 leads to the formation of a boundary layer below the gas-liquid interface, which expands diffusively over time. After some time, this diffusive layer is destabilized into denser fingers sinking downward in the gravity field.

Considerable differences in the convective and reactive dynamics and in their timescales are observed when the concentration of $Ca(OH)_2$ is varied. First, the time at which the instability appears decreases when the concentration of $Ca(OH)_2$ increases. Indeed, at $t = 150$ s, many small fingers have already formed in the most concentrated solutions of $Ca(OH)_2$ whereas less concentrated solutions are still in the diffusive stage. Another important difference concerns the production of precipitate due to the reaction between CO_3^{2-} and Ca^{2+} ions present in the aqueous solution. No precipitate is observed in $Ca(OH)_2$ solutions of concentration $< \times 10^{-3}$ M. For the 10^{-4} M solution, the development of fingers is similar to the one observed in water [7]. In 5×10^{-4} and 10^{-3} M solutions, the morphology of fingers is different. As compared to the less reactive case, fingers are wider and more clearly defined in intermediate $Ca(OH)_2$ concentrations.

In contrast, if the concentration of $Ca(OH)_2$ is larger than 10^{-3} M, solid $CaCO_3$ particles are quickly formed and create a multitude of small black fingers characterised by a short wavelength (Fig. 2). These solid particles settle down, inducing vigorous convection in the form of fingers
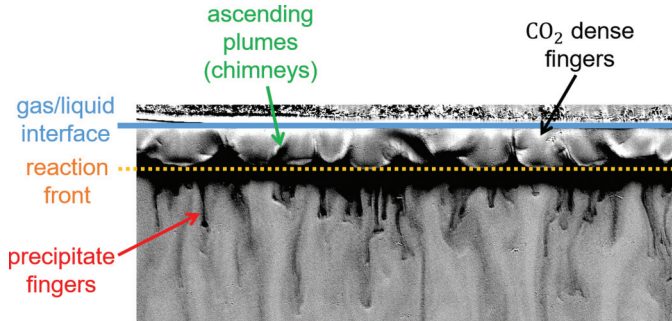
FIG. 3. Enlargement of the precipitation-driven convective pattern at $t = 600$ s in a solution of Ca(OH)$_2$ 5×10^{-3} M (see red rectangle in Fig. 2). The main characteristics of the convective dynamics are highlighted: The gas-liquid interface where gaseous CO$_2$ dissolves from above; the reaction front indicating the zone where the reaction rate is the largest; denser CO$_2$ fingers just below the gas-liquid interface; ascending plumes, driven by an upward flow generated by chemical reactions and evacuated through rising small chimneys appearing at the upper limit of the reaction front; and precipitate fingers, containing solid CaCO$_3$ particles sinking below the reaction front. The field of view is 4.0×1.5 cm.

mixing denser fluid and solid precipitate sinking in the aqueous phase. These fingers interact with each other, leading to a coarsening over time. After roughly 5 min, the reaction front becomes visible as a thick black horizontal line moving slowly away from the gas-liquid interface toward the bulk of the solution (Fig. 3). This reaction front indicates the region where the reaction rate is the largest and hence where the production of the solid precipitate is the highest. We see that, in those strongly reactive solutions, the dynamics is clearly driven by precipitation processes.

Although some precipitate sediments on the glass plates of the cell behind the reaction front, solid particles are essentially produced at the advancing reaction front and sink downwards as fingers, with a trajectory influenced by the flow generated by other convective fingers (Fig. 3). On the upper part of the reaction front, some plumes are also seen to rise upward, and an upward flow is evacuated through these small chimneys. In time, those chimneys move laterally and often merge to form larger ascending structures. These chimneys are suspected to be due to a local decrease in density inducing the less dense fluid to rise from the reaction front. This decrease can be due to the consumption of the reactants present in solution to produce locally denser solid particles that sink, inducing a smaller contribution of chemicals to the density of the liquid phase. Heat effects related to the exothermicity of the reaction can also appear locally and decrease the density. Note that thermal effects are usually of smaller amplitude than solutal ones in reactive convective dissolution [37]. Nevertheless, both solutal and thermal effects contribute to the rising of the plumes and it is difficult here to quantify their relative contribution.

Just below the gas-liquid interface, CO$_2$ continues to dissolve over time, still producing denser CO$_2$-rich aqueous fingers sinking toward the reaction front which sustains the precipitation process. The association of CO$_2$ fingers sinking downward from the interface and of plumes rising from the reaction front forms small convection rolls in the intermediate fluid layer of growing extension. These convection rolls weaken in time as the reaction front gradually moves away from the interface. All these features are highlighted in Fig. 3. To better appreciate the development of the precipitation pattern appearing in solutions of Ca(OH)$_2$ 5×10^{-3} and 10^{-2} M, the dynamics recorded with the second camera, i.e., with a wider field of view and no Schlieren effect, is displayed in Fig. 4.

This direct view clearly shows the precipitate left on the walls of the cell behind the downward-moving reaction front. This pattern on the wall reflects a memory of the convective cells which have brought the reactants into contact. Later on, it is progressively redissolved from above by the continuous intake of CO$_2$ which acidifies the area above the reaction front.
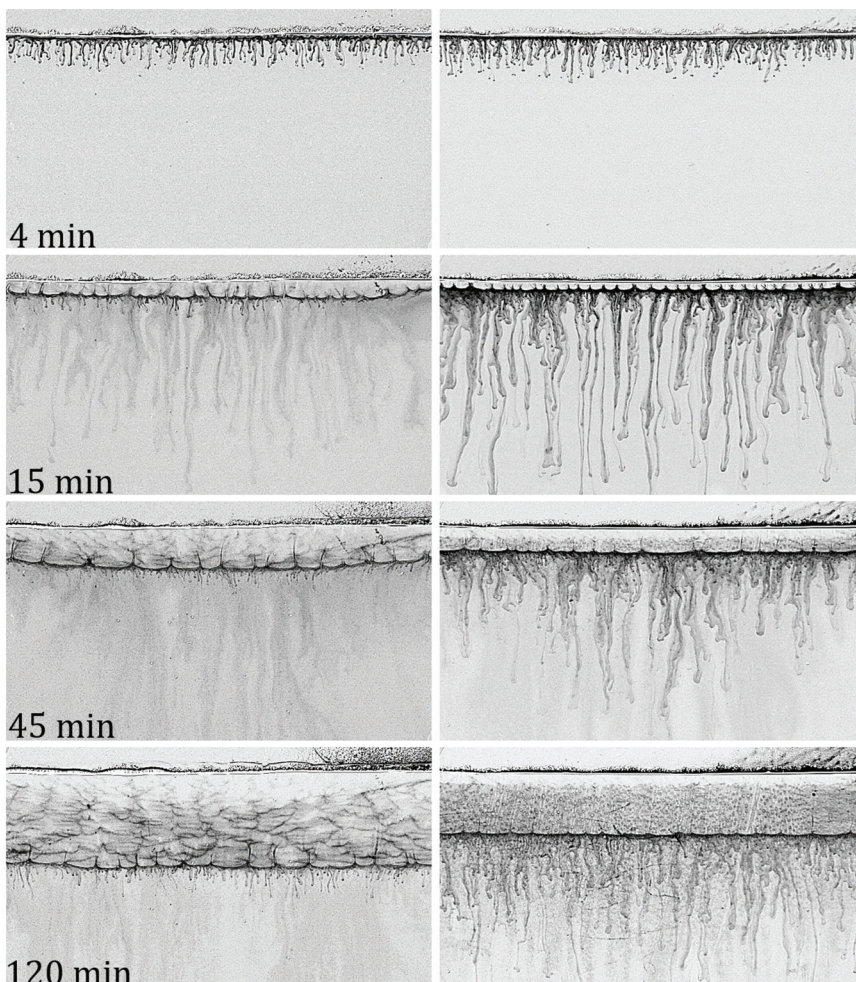
FIG. 4. Direct view of the temporal development (from top to bottom) of precipitation-driven dynamics in $Ca(OH)_2$ solutions in concentrations 5×10^{-3} M (left) and 10^{-2} M (right). The field of view is 13.3×7.5 cm.

Note that although more precipitate seems to be produced over time in the more concentrated solution, the reaction front propagates more quickly if the concentration of $Ca(OH)_2$ is intermediate. This difference will be further quantified in Sec. III D.

B. Horizontal space-time maps

The impact of varying the reactant concentration on the convective dynamics can be appreciated on space-time maps, plotting the dynamics on a line as a function of time. Figure 5 highlights the different positions selected to construct the various space-time maps. Figure 6 shows a comparison of space-time maps obtained during 115 min in water [7] and in different concentrations of $Ca(OH)_2$. Those maps are obtained by plotting in the course of time pixel intensities along the horizontal line 3 mm below the gas-liquid interface (see Fig. 5, red line 1). The movement of miscible fingers just below the gas-liquid interface highlights the drastic change of dynamics in solutions of $Ca(OH)_2$ 5×10^{-3} and 10^{-2} M where precipitation processes come into play.
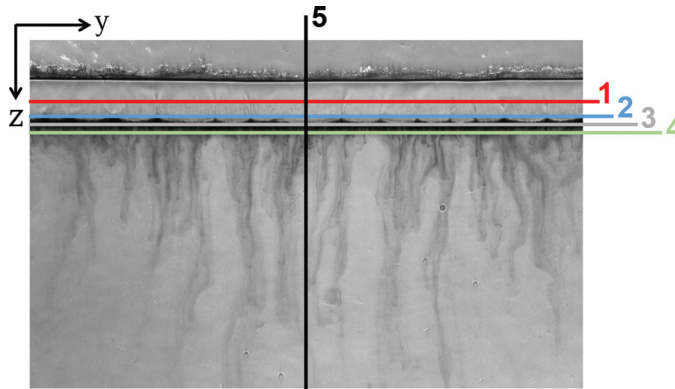
FIG. 5. Lines chosen to draw space-time maps: (1) 3 mm below the interface; (2) 1.3 mm above the reaction front; (3) position of the reaction front; (4) 1.3 mm below the reaction front; and (5) vertical line at the center of the image.

In less concentrated calcium hydroxide solutions [Figs. 6(b)–6(d)], the dynamics of finger bases near the interface is similar to the one observed in water [Fig. 6(a)], described previously [7]. Fingers appear after some time and first grow in the vertical direction before starting interacting with each other, inducing a horizontal drift. Eventually, they merge with one or several neighbors, which increases the wavelength of the convective pattern. Then, a reignition process of repetitive finger births and merging takes place until the end of the experiment. The reignition period of fingers is similar in water and in the two lowest concentrations of $Ca(OH)_2$ [Figs. 6(a)–6(c)] and is about 200 s. In 10^{-3} M solutions [Fig. 6(d)], the dynamics is observed to be more heterogeneous in the reignition phase as protofingers do not appear at the same position along the upper interface and the time interval between two finger births is variable. From this general point of view, we see that although the contrast slightly changes due to lateral diffusion of fingers, the convective dynamics near the interface is similar in water and in solutions of $Ca(OH)_2$ in the range of concentration 10^{-4} to 10^{-3} M. In more concentrated solutions [Figs. 6(e) and 6(f)], many small precipitate fingers rapidly develop during a short period of time. Then the reaction front appears, followed by the development of some ascending plumes. Once the local agitation associated to the passage of the reaction front is over, a new convective pattern formed of aqueous fingers establishes again below the gas-liquid interface. We observe that this second type of dynamics typically resembles the one developing in water. This is is due to the fact that, once the reaction front has moved downward, gaseous CO_2 continues to dissolve in this nonreactive region above the reaction front where $Ca(OH)_2$ has been consumed by the chemical reaction. Figures 6(e) and 6(f) also evidence the slower progression of the reaction front in the most concentrated of the two solutions. As explained theoretically [38–41], this is due to the fact that, if the reactant dissolved in the host phase is more concentrated, more CO_2 will have to react with it in order to move the same distance.

C. Space-time maps around the reaction front

As different convective dynamics (rising plumes versus sinking precipitate) are seen on both sides of the reaction front, it is also convenient to draw horizontal space-time maps of the dynamics near this downward-moving front. For this purpose, we follow the position of the front in time, and successively plot pixel intensities along a horizontal line respectively 1.3 mm above and 1.3 mm below the reaction front (see Fig. 5). This process leads to very distinct space-time maps, as depicted in Fig. 7, and allows us to compare the dynamics generated by the sinking of solid particles below the precipitation front with the one due to the ascending plumes above it.
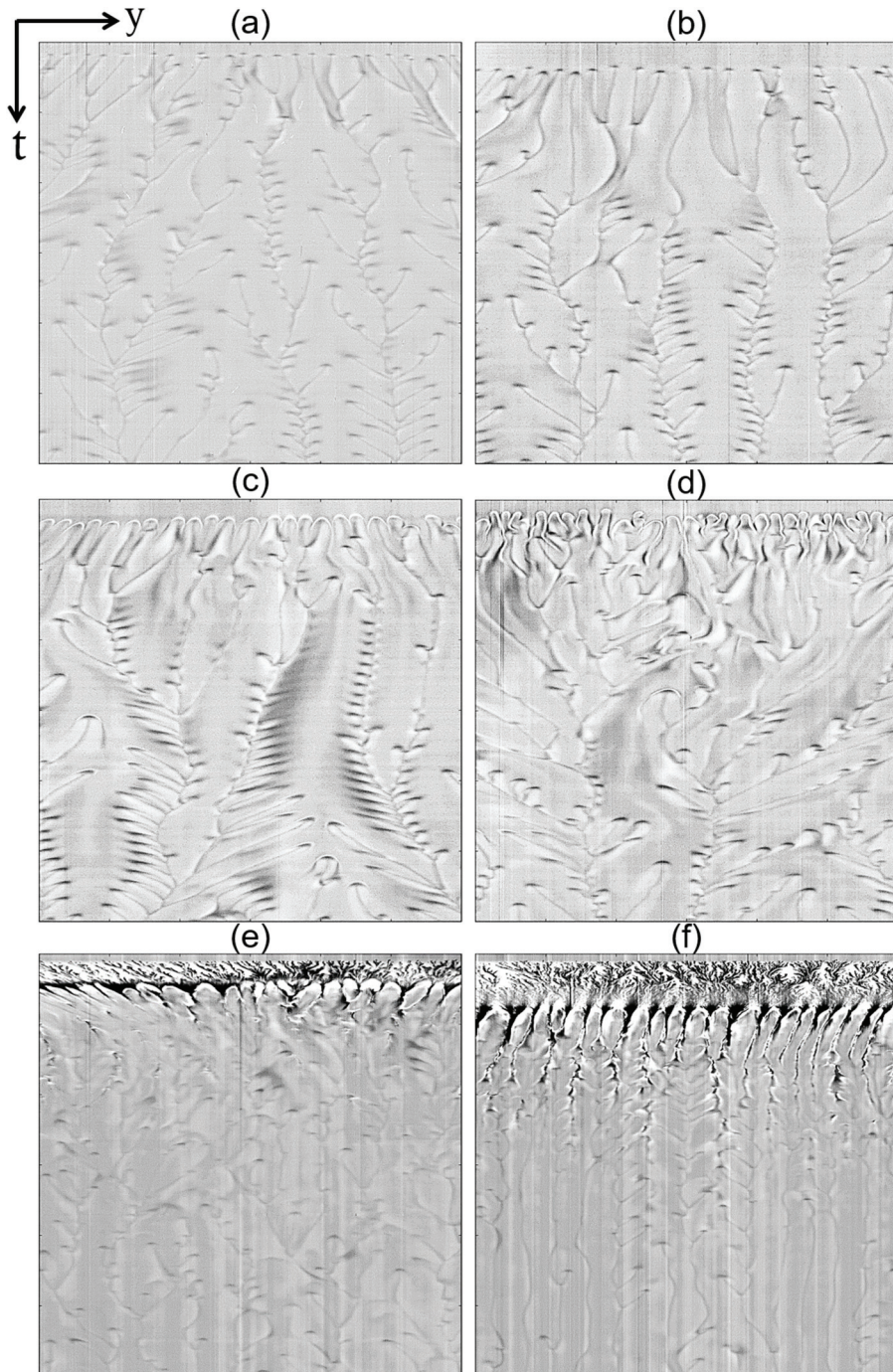
FIG. 6. Space-time maps of the dynamics on a horizontal line 3 mm below the gas-liquid interface as a function of time in (a) water [7] and in Ca(OH)$_2$ solutions of concentration (b) 10^{-4}, (c) 5×10^{-4}, (d) 10^{-3}, (e) 5×10^{-3}, and (f) 10^{-2} M. The horizontal length is 8.8 cm and the time resolution is 10 s. Time is running downward and the final time is 115 min.
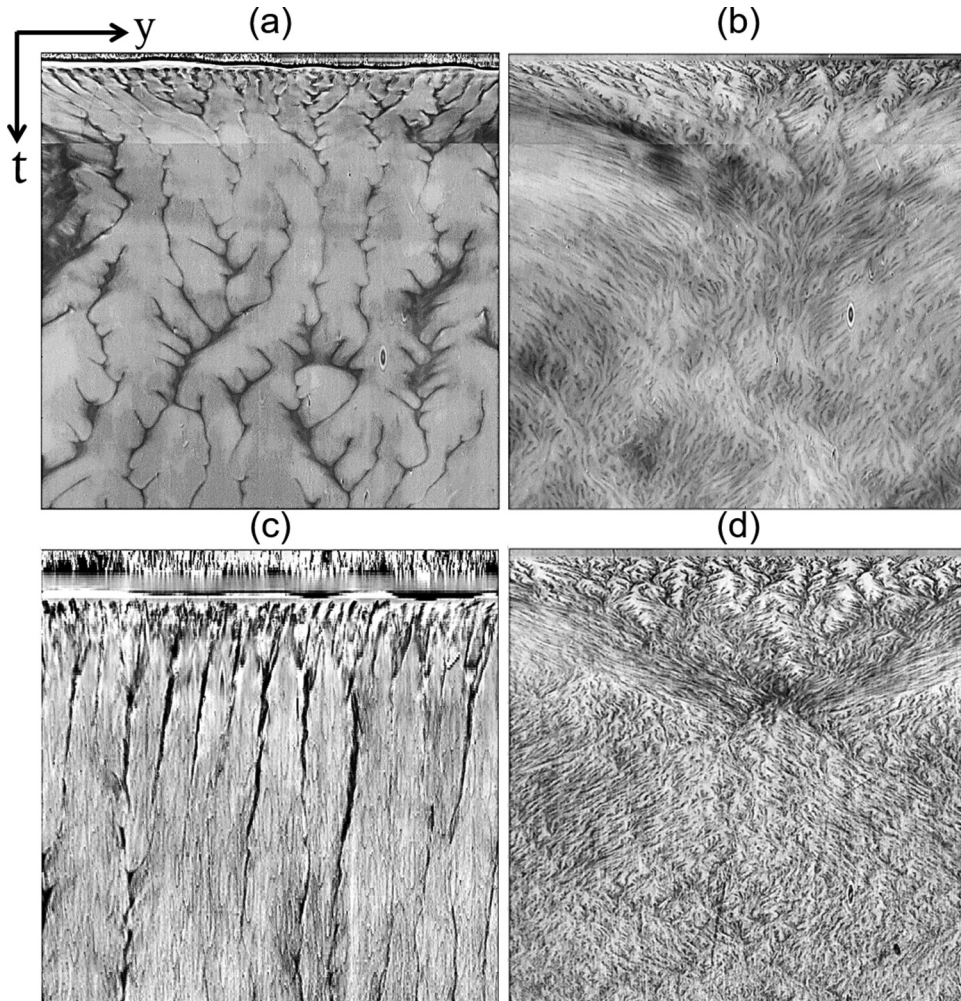
FIG. 7. Space-time maps of $Ca(OH)_2$ 5×10^{-3} M (a) above the reaction front and (b) below the reaction front. Space-time map of $Ca(OH)_2$ 10^{-2} M (c) above the reaction front and (d) below the reaction front. In each case, the horizontal length is 8.8 cm. Time is running downward up to 146 min.

The first part of the space-time maps above the reaction front [Figs. 7(a) and 7(c)] has no physical meaning. Indeed, with the reaction front starting at the gas-liquid interface at the beginning of the experiment, the position of the line 1.3 mm above the reaction front (line 2 on Fig. 5) is initially situated above the gas-liquid interface where nothing is detected. Then, as the reaction front moves away from the interface and travels downward, information on the convective dynamics above the reaction front progressively appears. After some time, the ascending plumes discussed in Sec. III A become observable. Therefore, Figs. 7(a) and 7(c) mostly show the movements of chimneys ejecting less dense rising plumes. We first observe a large number of plumes (≈ 40 in both cases) which rapidly start to merge. Then, the behavior of chimneys depends on the concentration of $Ca(OH)_2$ in solution. In the 5×10^{-3} M solution [Fig. 7(a)], the upward flow appears at random places and features large lateral movements. The ascending plumes created by chemical reactions at the front move toward each other before merging. In contrast, in the 10^{-2} M solution [Fig. 7(c)] we observe that the position of chimneys remains constant over time with relatively small lateral movements and that merging processes do not occur as frequently.
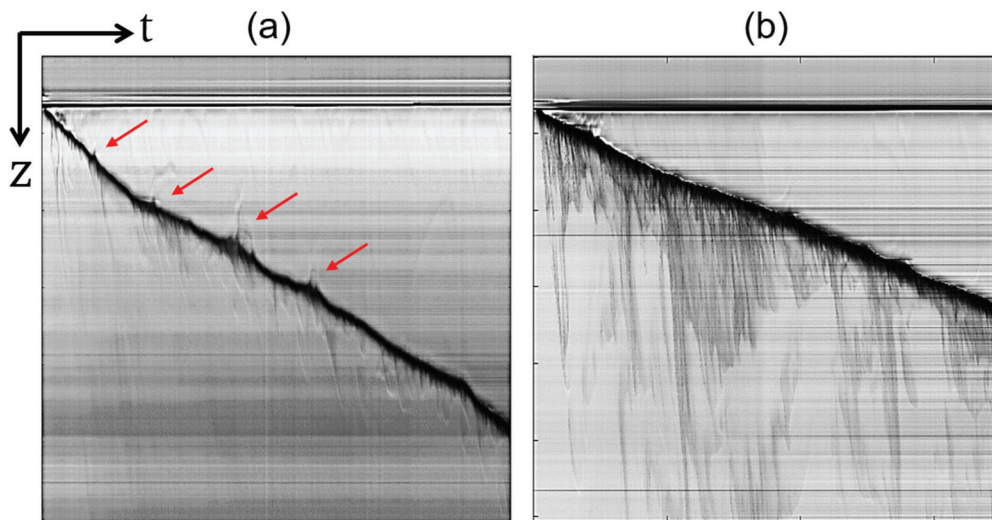
FIG. 8. Space-time maps of the dynamics along the vertical line at the center of pictures in solutions of $Ca(OH)_2$ (a) 5×10^{-3} M and (b) 10^{-2} M. Arrows indicate the location of some ascending plumes. Time is running horizontally, with a final time of 146 min. The vertical length is 5.5 cm.

This means that upward flows are here produced in preferential positions above the reaction front.

Below the reaction front, the dynamics shown by Figs. 7(b) and 7(d) is totally different. The space-time maps demonstrate the active production of many solid particles sinking in fingers and that convection does not weaken over the time period considered here (146 min). The only difference when the concentration of $Ca(OH)_2$ is increased is the smaller wavelength of the solid pattern [Fig. 7(d)], which indicates that more precipitate fingers are produced over time in more concentrated solutions. We finally note that a global lateral flow toward the center of the cell is here clearly visible during the first half of the time.

D. Vertical space-time maps

A different point of view on the dynamics is provided by the vertical space-time maps presented in Fig. 8, obtained by plotting the temporal evolution of pixel intensities along the vertical line at the center of images (see Fig. 5, black line 5). On these space-time maps, the interface is the horizontal line in the upper part of the image, and the reaction front, which is moving downward in time, is the thick black diagonal line. In Fig. 8(a), a few ascending plumes are seen in some places above the reaction front (see red arrows on figure). Sinking precipitate fingers are also observed below the reaction front as a dark shadow in both maps. We note that the production of sinking fingers at this central zone of the map is irregular in both cases and is more intense in the most concentrated solution [Fig. 8(b)].

On such space-time maps, the mean vertical speed v_f of the reaction front can be measured as the slope of the front position versus time averaged over several positions. We find $v_f = (0.3 \pm 0.1)$ and (0.17 ± 0.01) mm/min for $Ca(OH)_2$ 5×10^{-3} and 10^{-2} M solutions, respectively. It is important to note that for this measure we selected the first slope appearing on the maps. Indeed, even if the speed of the reaction front was observed to be constant in time in most of the experiments considered here, the reaction front in some cases slows down after some time, particularly in 5×10^{-3} M experiments longer than 30 min. This slowdown of the front is clearly observable in Fig. 8(a), for which we measure a speed of 0.38 mm/min during the first part of the experiment, followed by a decrease of
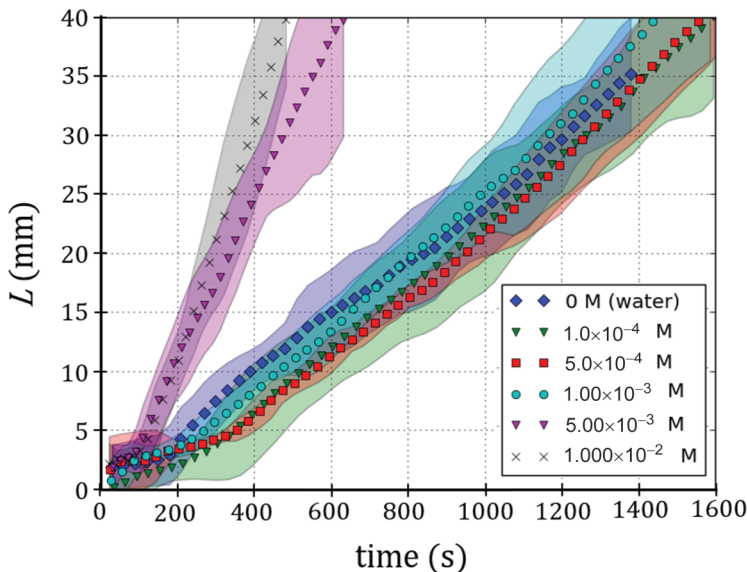
FIG. 9. Temporal evolution of the mixing length L in water and in solutions of $Ca(OH)_2$ of various concentrations. Each curve represents the average on several experiments. The shaded zones around the curves represent the associated double standard deviation.

almost 50% to 0.22 mm/min. This deceleration of the reaction front was not observed in 10^{-2} M solutions.

E. Mixing lengths

To further analyze the impact of the mineralization reaction on convection, we compare the temporal evolution of the mixing length L in water and in solutions of $Ca(OH)_2$ of various concentrations (Fig. 9). Here L is the distance between the interface and the tip of the longest finger, averaged over several experiments at the same concentration.

Figure 9 shows that the evolution of L is qualitatively similar in all cases. It first grows diffusively followed by a linear increase after the onset of convection, the slope of which gives the vertical finger velocity v. Figure 10 giving v as a function of the $Ca(OH)_2$ concentration shows that two different regimes are observed depending on the presence of solid particles. For $Ca(OH)_2$ concentrations smaller or equal to 10^{-3} M, we remain below the solubility limit of $CaCO_3$. Hence the fingers containing the denser liquid solution sink with a vertical velocity in the range 1.6–1.8 mm/min, similar to the one measured in pure water [7]. Once the concentration of reactant is large enough such that the amount of $CaCO_3$ produced is above its solubility limit [i.e., for $Ca(OH)_2$ concentrations larger than 10^{-3} M], solid particles are formed. As the amount of $CaCO_3$ particles produced by the reaction is proportional to $[Ca(OH)_2]$, the concentration of the hydroxyde reactant, we can suppose that the density difference $\Delta\rho$ between the density of the solid particles suspension and that of the bulk liquid increases linearly with $[Ca(OH)_2]$. As a result, the settling velocity v which is linearly proportional to $\Delta\rho$ increases linearly with $[Ca(OH)_2]$ in the case of precipitation, as observed in Fig. 10.

This shows that the sinking speed of solid particles is larger than that of aqueous convective fingers. It suggests that, in addition to the mineralization advantage for safety of CO_2 sequestration, convective transport is also more efficient to drag the solid carbonate down in the aquifer when a solid precipitate is formed.
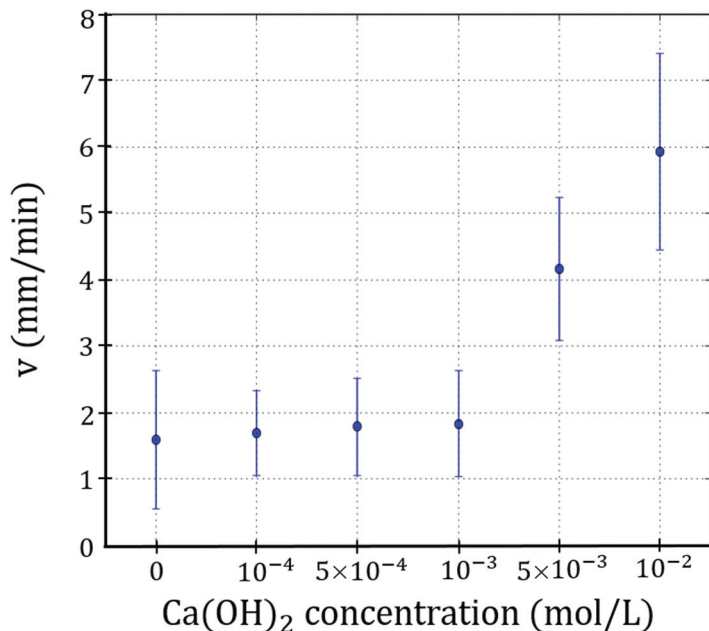
FIG. 10. Averaged finger velocities as a function of $Ca(OH)_2$ concentration, computed from the slope of the temporal evolution of mixing lengths. Error bars represent the double of standard deviation.

F. Fourier analysis

To characterize the development of fingers at the onset of convection, the full contour of the contrasted zone in which CO_2 has dissolved is detected on each experimental image and is next analyzed by means of Fourier transform to extract the characteristic wavelength of the instability. For a given time, all Fourier spectra obtained for the different experiments of a same concentration are averaged. In Fig. 11, the spectra for different concentrations of $Ca(OH)_2$ are compared after a few minutes. We see that, for smaller concentrations, the dominant wavelength is close to 4 mm, the same value as in pure water [7]. Analyzing the growth rate of the amplitude as a function of concentration shows that the destabilization of the diffusive layer is much faster in the presence of the precipitation reaction as evidenced by the larger amplitudes at similar times. This evidences the fact that, in $Ca(OH)_2$ solutions, convection appears sooner when the concentration of the hydroxyde reactant is increased, as also seen in Figs. 2 and 9.

G. pH changes

In order to obtain information on the evolution of pH in the aqueous solution due to the presence of acidic dissolved CO_2, additional experiments have been performed with the use of a universal color indicator, the color of which changes gradually in the range of pH 4–10 (yellow to blue). Figure 12 shows precipitation patterns observed during the dissolution of CO_2 in a solution of $Ca(OH)_2$ 5×10^{-3} M. As the initial pH of the host solution is larger than 10, the initial color of the basic solution is purple. The first solid fingers appearing at the onset of convection are also purple but darker than the bulk solution, which indicates that in the early stages of the experiment, the pH of the aqueous solution does not decrease significantly. However, the color of the solution progressively turns to green in the region near the gas-liquid interface, in the convective rolls developing above the reaction front. This means that in this intermediate region, the pH decreases to values close to 6. As time progresses, this acidic area grows as the reaction front travels downward. Below the reaction front, the color of the solution does not change over time, meaning that the pH of the invaded bulk
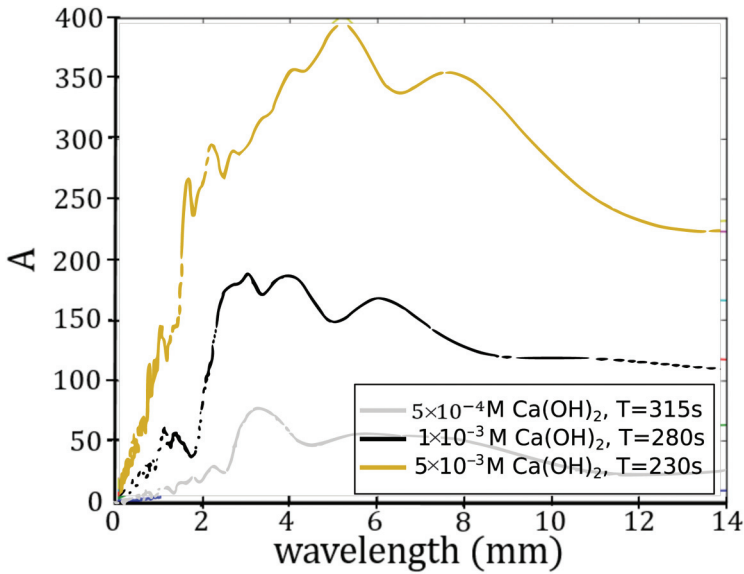
FIG. 11. Comparison of the Fourier spectra for solutions of $Ca(OH)_2$ 5×10^{-4}, 10^{-3}, and 5×10^{-3} M.

solution remains constant. We also note that the plumes rising from the reaction front toward the gas-liquid interface are small basic purple channels in the green acidic area (see circled area in Fig. 12). It suggests that those plumes are generated by the penetration and ascension of the basic bulk solution toward the gas-liquid interface.
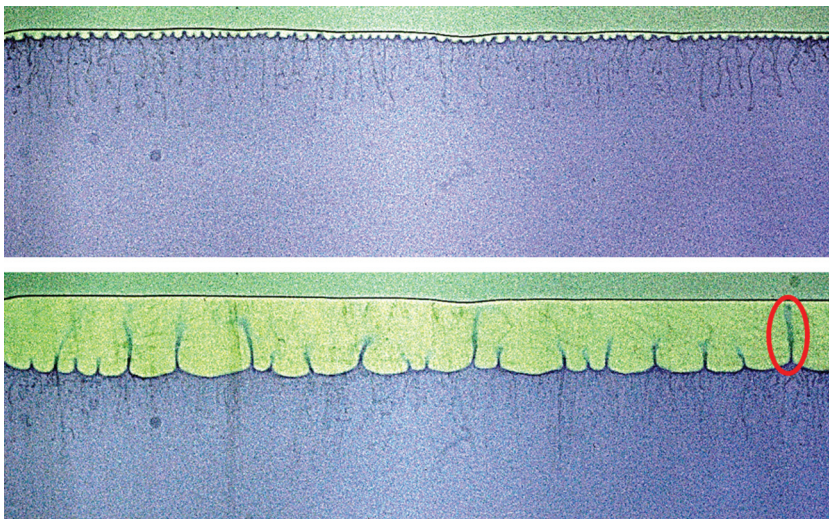

FIG. 12. Visualization of pH changes in a solution of $Ca(OH)_2$ 5×10^{-3} M by a universal color indicator at $t = 5$ min (top) and $t = 48$ min (bottom). The contrast and brightness of images have been modified to improve color contrasts, which explains the green area above the gas-liquid interface. The red circled area indicates a rising basic purple channel in the green intermediate area. The field of view is 16 cm wide.
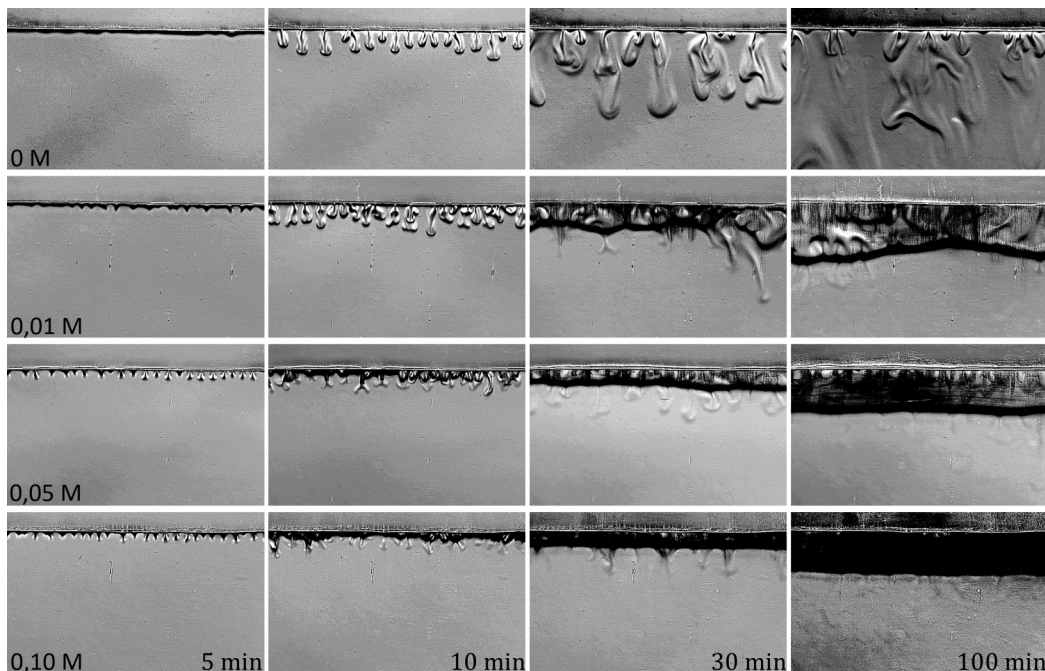
FIG. 13. Temporal development of the convective instability generated by the dissolution of CO_2 in $CaCl_2$ solutions of various concentration. The field of view is 8.8×5.5 cm.

IV. PRECIPITATION-DRIVEN INSTABILITIES IN SOLUTIONS OF $CaCl_2$

In order to investigate precipitation-driven processes in a different reactive environment, we now turn to the study of the convective dynamics developing in solutions of the salt $CaCl_2$. We recall that the solvent used for $CaCl_2$ experiments is a 0.0125 M borax solution to mimic the buffering capacity of some geological reservoirs. In this case, the initial pH of the solution is close to 9. We will also investigate the use of a different buffer and compare this to the case without a buffer in Sec. IV E.

A. Phenomenology

A comparison of the dynamics developing upon CO_2 dissolution in $CaCl_2$ solutions of concentration 0–0.1 M is shown in Fig. 13. In this case, the impact of the precipitation reaction on the convective dynamics is different from the one previously observed in $Ca(OH)_2$ solutions. In (pure) borax solutions (i.e., 0 M), no precipitate is formed and a typical buoyancy-driven convective pattern develops over time, which is slightly different from the one developing in water [7]. More details are in Sec. IV E.

In contrast, the presence of $CaCl_2$ in the solution and its reaction with dissolved CO_2 seems to hinder the convective dynamics. After a diffusive regime and an onset of convection comparable in space and time to the one observed in borax, precipitation develops in the presence of $CaCl_2$, which strongly modifies the subsequent growth of aqueous fingers. First, solid particles of $CaCO_3$ are seen to be produced inside the growing fingers and to stick to the glass plates of the Hele-Shaw cell. As soon as the precipitate is formed, the initially growing fingers become less dense, which causes them to rise back toward the gas-liquid interface, leaving behind immobile solid particles deposited on the walls of the cell. In parallel, precipitation reactions below the interface lead to the formation
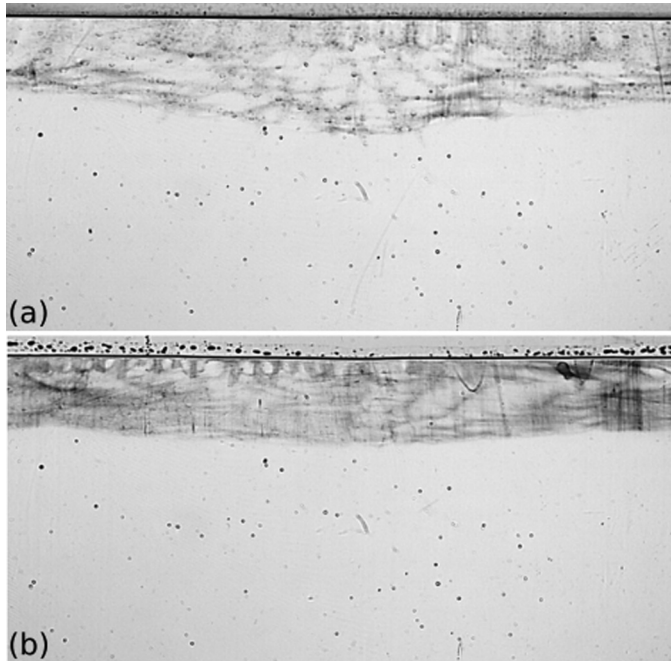
FIG. 14. Direct view of precipitation pattern in solutions of $CaCl_2$ (a) 0.01 and (b) 0.10 M after 2 h of experiment. The field of view is 13.5×6.6 cm.

of a continuous reaction front, appearing as a thick black layer which slowly progresses downward over time.

Once the reaction front is formed, precipitation seems to occur only around it and very distinct dynamics develop below and above it. Below the front, contrast differences are low and the dynamics is barely observable, which means that the density gradients in this region are weak. Nevertheless, we see a few denser liquid fingers which sink slowly downward. They fade in time and progressively disappear. These fingers take sometimes specific antenna shape, reminding us of mixed mode fingers, previously observed when a Rayleigh-Taylor instability interacts with double diffusive effects [40,42]. Sometimes, a small amount of precipitate is found in some places just below the reaction front, but this lower area is generally free from precipitate or contains a very low amount of it. Above the reaction front, similarly to the convective rolls appearing in $Ca(OH)_2$ experiments, we observe convective motions driven by, on the top, the convective dissolution of CO_2 at the gas-liquid interface and, above the reaction front, by plumes rising toward the interface. As compared to the case of $Ca(OH)_2$, convective rolls are difficult to observe here because convection is weaker and the precipitation pattern on the foreground glass plate interferes with our visualization of the convection occurring behind. This effect is particularly important in the most concentrated solutions of $CaCl_2$ where the area between the gas-liquid interface and the precipitation front is completely dark. Note that in reality the precipitate is colorless (i.e., white) but appears black on Schlieren images because of the strong light scattering induced by the solid particles. Finally, as time progresses, the precipitation front slowly moves toward the bulk of the solution, leaving behind a stratification of solid particles sticking to the walls of the cell. Unlike $Ca(OH)_2$ experiments, no redissolution of the precipitation pattern was observed.

In order to evaluate whether the concentration of $CaCl_2$ has an influence on the dynamics, we compare in Fig. 14 the precipitation pattern at the end of experiments in $CaCl_2$ solutions 0.01 M and 0.10 M imaged with the second camera, i.e., without Schlieren effect. This allows us to attenuate the contrasts induced by the strong refraction of solid particles and observe the precipitation patterns

more precisely. We observe that, even if the progression of the precipitation front is similar in both solutions, it appears that more precipitate has been deposited on the glass of the cell in the most concentrated solution of $CaCl_2$ where the solid pattern is darker and more evenly distributed.

To sum up, the production of solid $CaCO_3$ upon reaction of dissolved CO_2 with $CaCl_2$ has an impact on the density of the aqueous solution. Indeed, immediately after the production of the solid precipitate, the flow of fingers rapidly changes as they are seen to rise back to the interface, which means that they become less dense than the surrounding solution. The precipitation front in $CaCl_2$ experiments acts as a stabilizing barrier which inhibits the transport of dissolved CO_2 in the bulk of the solution. Moreover, changing the concentration of $CaCl_2$ in the solution does not seem to have a significant impact on the development of the convective dynamics. However, a closer comparison of precipitation patterns suggests that more precipitate is produced above the reaction front in the most concentrated solutions of $CaCl_2$ (Fig. 14). In order to compare the dynamics from a more general point of view, we analyze in the following sections the spatiotemporal diagrams of experiments in solutions of borax and $CaCl_2$ of various concentrations.

B. Horizontal space-time maps

Figure 15 compares the horizontal space-time maps (taken 3 mm below the interface) of 100-min experiments in solutions of borax and $CaCl_2$ 0, 0.01, 0.05, and 0.10 M. In the pure borax solution [Fig. 15(a)], the phenomenology of fingers is similar to the one observed in water [Fig. 6(a)]. Fewer fingers are present at the onset of convection in borax where we count 17 fingers, instead of the 21 found in the space-time map of water. In solutions of $CaCl_2$, we first see the fingers developing over a short time after the onset of convection, and then the black precipitation front appears at a time similar in all $CaCl_2$ solutions. After the passage of the front, the dynamics in the region near the gas-liquid interface is mostly driven by the dissolution of CO_2. Even if the map is blurry, especially the one of $CaCl_2$ 0.10 M [Fig. 15(d)], we distinguish a repetitive production of fingers which travel along the interface to merge with other neighboring fingers. This demonstrates that gaseous CO_2 continues to dissolve at the interface, generating buoyancy-driven convection which promotes the transport of the dissolved CO_2 to the reaction front where it reacts with $CaCl_2$. Finally, we note that the wavelength of fingers at the onset of convection does not change significantly with the concentration of reactant in solution, although fewer fingers are seen in borax than in $CaCl_2$ solutions where we count $\approx$21–22 fingers [Figs. 15(b)–15(d)].

C. Vertical space-time maps

Our observations on Figs. 13 and 15 suggest that, by opposition to $Ca(OH)_2$ experiments, the reactant concentration does not affect significantly the evolution of the precipitation front in $CaCl_2$ solutions. This can also be seen on vertical space-time maps obtained in $CaCl_2$ solutions of concentration 0.01, 0.025, and 0.10 M (Fig. 16).

For the lowest concentrations of $CaCl_2$ [Figs. 16(a) and 16(b)], the convection occurring in the zone between the gas-liquid interface and the reaction front is clearly visible. Below the gas-liquid interface, fingers are seen to emerge over time, especially in 0.025 M solution [Fig. 16(b)], where a series of fingers is produced in the horizontal direction of the space-time map. Those two maps also show some plumes rising from the reaction front at this central position of the images. In the largest concentration of $CaCl_2$ [Fig. 16(c)], however, the precipitation pattern is too dark and hides the convection developing behind the front.

The vertical progression of the reaction front is similar in the three cases considered in Fig. 16. From the vertical maps, we have computed the vertical velocities v_f of the reaction front in the various solutions of $CaCl_2$. As in most experiments, the reaction front is irregular, so we create 20 vertical space-time maps at regular positions along the image and average the 20 computed front velocities. The averaged velocities v_f obtained for the different concentrations of $CaCl_2$ were statistically equivalent and equal to (0.14 ± 0.06) mm/min.
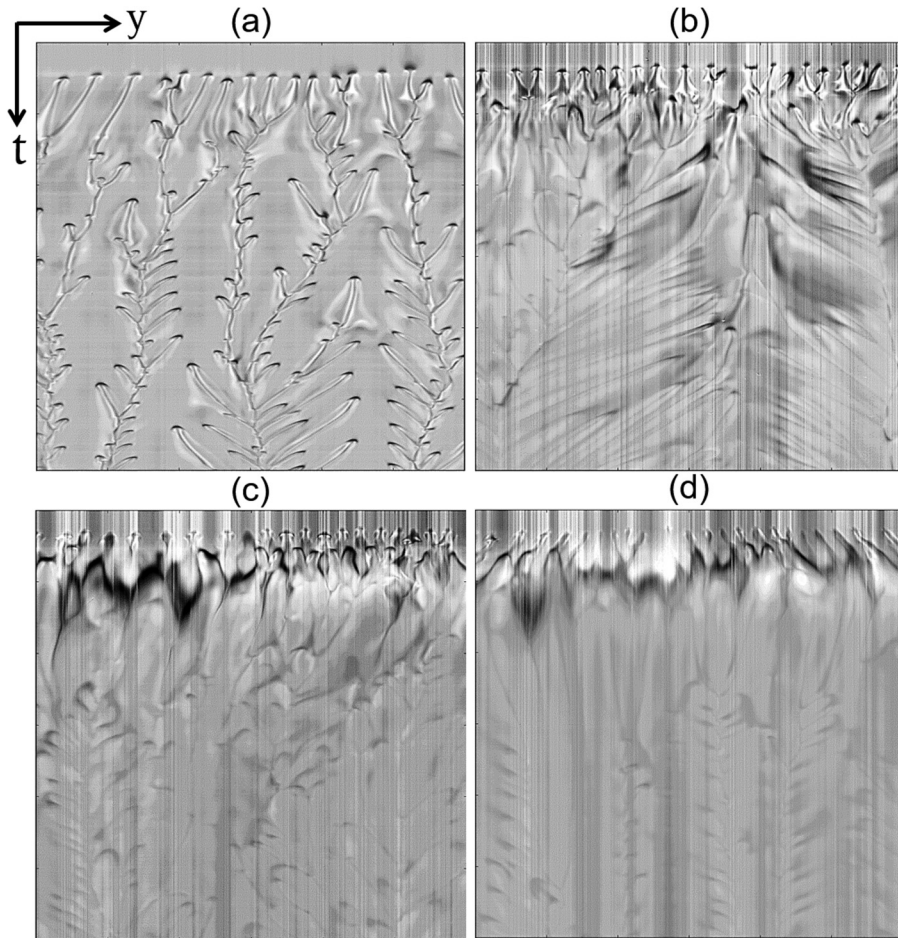
FIG. 15. Space-time maps of the dynamics along a horizontal line 3 mm below the interface in solutions of borax alone (a) and of borax containing $CaCl_2$ 0.01 (b), 0.05 (c), and 0.10 M (d). The width is 8.8 cm. Time is running downward with a maximum of 100 min.
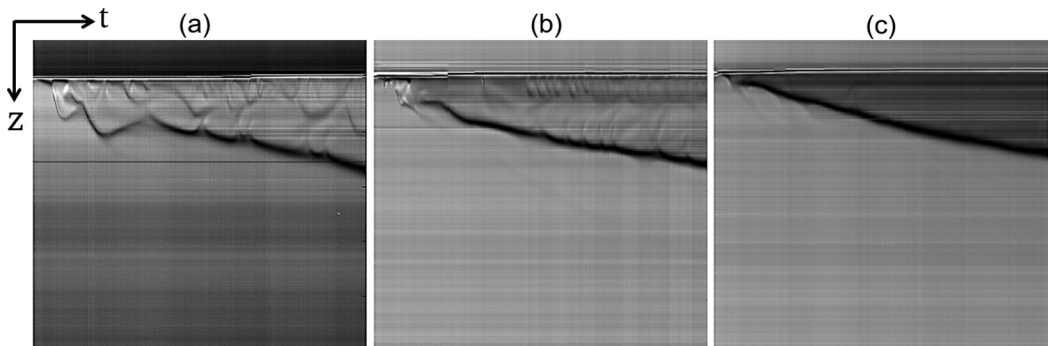

FIG. 16. Vertical space-time maps of the dynamics at the center of pictures in solutions of $CaCl_2$ (a) 0.01; (b) 0.025; and (c) 0.10 M. The height is 5.5 cm. Time is running horizontally, and the maximum time is 100 min.
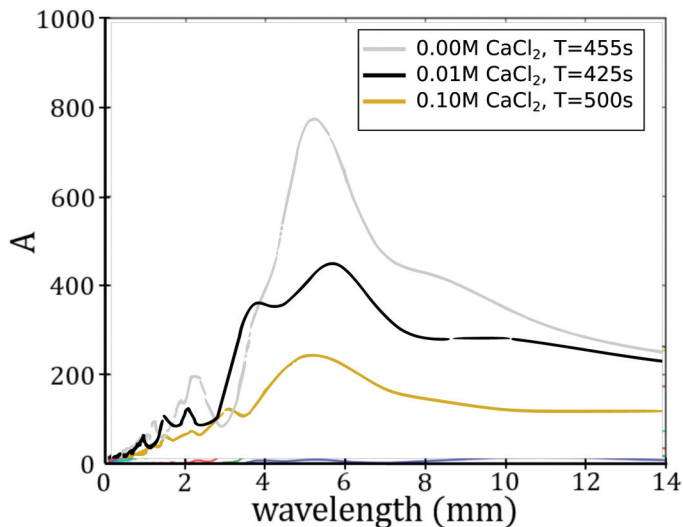
FIG. 17. Comparison of the Fourier spectra for borax and varying $CaCl_2$ concentrations (0, 0.01, and 0.10 M).

D. Fourier analysis

To further quantify the wavelength of the instability as a function of $CaCl_2$ concentration, we compute the Fourier spectra characterizing the convective destabilization of the diffusive layer. In Fig. 17, three representative spectra are superimposed for solutions of borax with 0, 0.01, and 0.1 M $CaCl_2$. Although the spectra are not extracted at the same instant, it is clear that the maximum amplitude is found in borax, where liquid fingers are not slowed down by precipitation processes. The maximum amplitude is associated to a wavelength close to 5 mm. In the two other solutions, the amplitude of the peak at similar times is smaller if the concentration of $CaCl_2$ is larger. This means that during the first 500 s of the experiment, fingers develop more rapidly in borax solutions than in $CaCl_2$ solutions. This is consistent with the patterns observed on the second column of Fig. 13, where, at $t = 10$ min, fingers have already started to disappear in $CaCl_2$ 0.10 M.

E. Impact of buffer on the convective dynamics

As previously mentioned, if experiments are performed without borax, i.e., in solutions of $CaCl_2$ only, the pH of the solution decreases immediately with CO_2 dissolution and no precipitate is observed during experiments. The impact of the buffer on the convective dynamics, however, is unclear as the possible interactions between boric acid and the species dissolved in the solution are difficult to determine. For this reason, we have also performed a few tests of CO_2 dissolution in solutions of glycine containing $CaCl_2$ to assess if the nature of the buffer affects the convective pattern developing in the solution.

The convective pattern imaged at $t = 10$ min in water, borax, and glycine in absence of $CaCl_2$ is presented in Fig. 18. As opposed to the water case, fingers developing in borax and glycine are easily detectable and well contrasted, which means that the density gradients at the origin of the instability are larger than in water. Even if the phenomenology of the convective dynamics is similar in the three solvents, the instability is seen to develop more quickly and with more fingers in glycine than in water, and seems to be slightly slower in borax. We count at the onset of convection 21, 17, and 35 fingers on 8.8 cm in water, borax, and glycine, respectively. Finally, note that the tip of fingers in borax is seen to enlarge considerably more than in water, which sometimes leads to tip splitting, which was not observed in water or glycine.
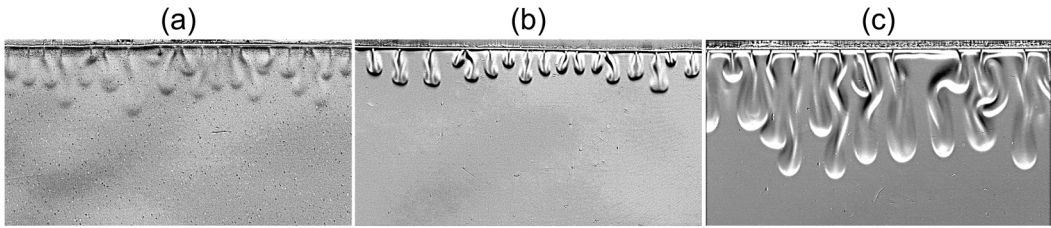
FIG. 18. Comparison of the fingering pattern observed with the Schlieren technique at $t = 10$ min in (a) water, (b) borax 0.0125 M, and (c) glycine 0.0125 M. The field of view is 8.8×5.5 cm.

We have next analyzed the convective pattern developing in glycine containing $CaCl_2$ in concentration 0.10 and 0.50 M. The convective dynamics is completely different from the one observed in borax. In glycine, the buoyancy-driven convection does not seem to be strongly affected by the presence of $CaCl_2$ as much less precipitate is formed over time. Figure 19 compares the precipitation patterns imaged at $t = 55$ min in glycine solutions containing $CaCl_2$ 0.10 M (left) and 0.50 M (right). The formation of solid particles was not observed at the beginning of experiments but rather after 15 min (in 0.50 M) to 30 min (in 0.10 M). No clear decrease of solution density was noticed after precipitation reactions. In this case, no precipitation front was observed as the solid particles form inside the convective fingers and are progressively deposited on the glass plates. If the concentration of $CaCl_2$ is increased, the precipitate appears sooner and the amount of precipitate at the end of the experiment is larger, as demonstrated by Fig. 19.

F. pH changes

To assess the efficiency of borax and glycine to maintain the pH of the solution to values close to 9 and resist to the acidification caused by CO_2 dissolution, the evolution of pH has been evaluated by means of a universal color indicator. Figure 20 shows a comparison of the patterns revealed by color changes of the indicator in borax and glycine solutions containing $CaCl_2$ 0.10 M. In both cases, the color of the initial solution is blue (pH $\approx$ 9). The case of CO_2 dissolution in borax alone [Fig. 20(a)] is similar to what has been previously observed in $Ca(OH)_2$ (Fig. 12), where the pH decrease is limited to the zone between the precipitation front and the gas-liquid interface. A few fingers, barely visible, develop below the precipitation front, which means that the low contrasted fingers observed on Schlieren images (Fig. 13) are only slightly acidic. In glycine, a yellow boundary layer emerges rapidly in the solution and is subsequently destabilized into yellow fingers growing over time, which demonstrates that the buffering capacity of glycine is not sufficient to mitigate the pH decrease
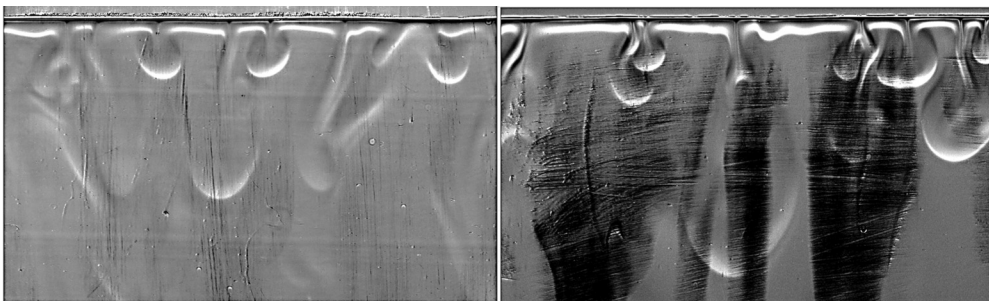

FIG. 19. Comparison of the fingering pattern observed at $t = 55$ min in glycine with $CaCl_2$ 0.10 M (left) and 0.50 M (right). Black zones correspond to solid precipitate which has sedimented on the walls of the cell. The field of view is 8.8×5.5 cm.
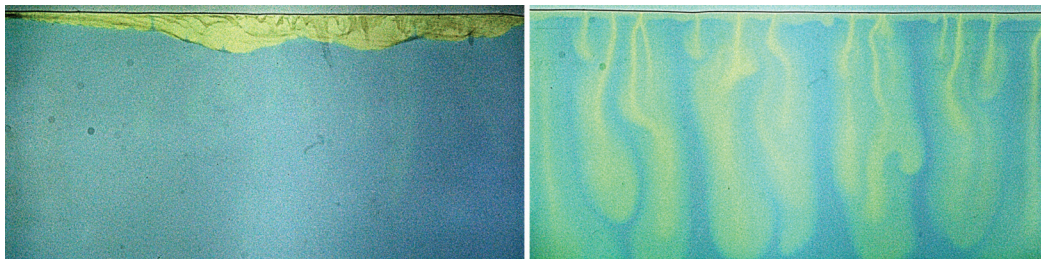
FIG. 20. Comparison of convection in a solution of $CaCl_2$ 0.10 M with a universal color indicator at $t =$ 50 min in borax 0.0125 M (left) and in glycine 0.0125 M (right). The field of view is 16 cm wide.

induced by CO_2 dissolution. This could justify the differences observed in the convective dynamics developing in borax and glycine and explain why the amount of precipitate found in glycine is low.

V. DISCUSSION

The interpretation of the complex convective patterns observed in the various reactive aqueous solutions is difficult as several parameters are expected to influence the interplay between precipitation processes and convective dissolution. Here, we will discuss two of them: the influence of pH on the occurence of the precipitation reaction and the possible influence of differential diffusivity on the appearance of fingers below the reaction front.

A. Influence of the pH of the aqueous solution

In the case of $Ca(OH)_2$ solutions, varying the concentration of the base in the host solution changes the initial pH of the solution, as seen in Table I. As a consequence, the initial concentration of bicarbonate HCO_3^- and carbonate CO_3^{2-} ions in the solution is different in the considered $Ca(OH)_2$ solutions of variable concentrations. For pH solutions ranging from 6 to 10, most of the dissolved CO_2 in the aqueous phase is in the form of bicarbonate ions HCO_3^- [43]. Carbonate ions CO_3^{2-} are only present in the solution if the pH is larger than 8. Therefore, the formation of $CaCO_3$ is only expected to occur if the pH of the solution is large enough. This was also found experimentally as below a critical $Ca(OH)_2$ concentration (close to 10^{-3} M), the pH decrease induced by CO_2 dissolution creates an acidic environment in the aqueous phase which prevents the precipitation of $CaCO_3$. In this case, convective aqueous fingers develop, driven by density gradients building up in the aqueous solution. In these diluted $Ca(OH)_2$ solutions, the concentration of the reactant does not affect significantly the growth of the convective instability but fingers appear wider if the concentration is increased, which suggests an influence of the diffusion coefficients of the dissolved species.

If the concentration of $Ca(OH)_2$ is large enough ($> 10^{-3}$ M), the solution remains basic even upon CO_2 dissolution, which favors the precipitation of carbonates. This leads to a distinct convective pattern, where the reaction-precipitation front is seen to move toward the bulk of the solution over time, leaving behind immobile solid particles on the walls of the Hele-Shaw cell. The convective dynamics developing above and below the reaction front are different as the density profile of the aqueous solution is nonmonotonic. Above the reaction front, convective rolls appear, driven by dense CO_2 aqueous fingers at the gas-liquid interface and by the plumes rising from the minimum in density at the upper part of the reaction front [40]. Below the reaction front, many precipitate fingers are produced over time and sink at a larger speed than liquid fingers toward the bulk of the solution, which intensifies convective motions in this lower region.

TABLE II. Solubility S, diffusion coefficient D, and solutal expansion coefficients α for the chemical species considered in this study. Diffusion coefficients were computed from Ref. [44], assuming that the solvent is water. The values of α for $CaCl_2$ were measured experimentally in borax solutions. This measure could not be performed for $Ca(OH)_2$ solutions and $CaCO_3$ as their solubility in water is too low.

Species	S (mol/l)	D (10^{-9} m^2/s)	α (10^{-2} l/mol)
CO_2	0.039	1.75	0.82
$Ca(OH)_2$	0.010	1.83	
$CaCl_2$	2.000	1.33	8.85
$CaCO_3$	7×10^{-5}	0.85	

On the other hand, the predominance of bicarbonate ions in the solution at intermediate pH could promote the formation of calcium bicarbonate ions $CaHCO_3^+$, following equilibrium (5). This species is probably dominant in experiments with $Ca(OH)_2$ in the range 10^{-4}–10^{-3} M, where the convective instability develops in the form of liquid fingers. However, the contributions of $CaHCO_3^+$ to the density of the solution or its diffusion coefficient are difficult to determine.

If we now consider $CaCl_2$ solutions, the problem is more complex as the aqueous solutions have been buffered to a pH of 9. As $CaCl_2$ is slightly acidic in water, increasing its concentration lowers the pH of the initial aqueous solution. This effect is smaller in borax buffer solutions than in water but is non-negligible, as seen in Table I. This decrease of pH when increasing $CaCl_2$ concentration does not seem to have an impact on the amount of precipitate produced during experiments but further quantification is necessary to clarify this point. In $CaCl_2$ solutions without borax, the dissolution of CO_2 in the solution does not lead to the formation of solid $CaCO_3$ as the pH is too acidic. In borax, the initial pH of the solution is close to 9, for which carbonate ions are present in the solution. The dissolution of CO_2 lowers the pH of the solution but this decrease is limited to the boundary layer below the gas-liquid interface. Indeed, as seen in the experiments performed with a color indicator (Fig. 20), the pH of the bulk solution below the reaction front remains constant over time and hence the production of $CaCO_3$ is possible at the reaction front where calcium and carbonate ions meet and react.

B. Influence of differential diffusivity

From Table II, we see that all species diffuse at different rates in the aqueous solution, which is known to influence the shape of the density profile in the host phase [38,40,41,45,46]. Although CO_2 and $Ca(OH)_2$ have quite similar diffusion coefficients, $CaCl_2$ diffuses more slowly than CO_2, which could lead to a nonmonotonic density profile in the host solution [40,41,47]. As a result, two distinct dynamics can develop above and below the reaction front. Above the reaction front, a convective instability sets in due to the unstable density gradient from the gas-liquid interface to the reaction front. However, the slower diffusion of the reactant in the host phase creates an accumulation zone below the reaction front, together with a depletion zone above the reaction front, which acts as a stabilizing barrier as the local density of the aqueous solution decreases. Below the reaction front, the small local maximum in density due to the accumulation of the reactant induces downward-sinking fingers [40,41,48]. These fingers take also antenna shapes due to differential diffusion effects [42]. However, convection remains weak as the density difference between the area just below the reaction front and the bulk of the solution is low. We also note that the diffusion coefficient of aqueous $CaCO_3$ is much smaller than those of the other species. Moreover, as its solubility in water is low (see Table II), we can consider in a first approximation that this species only exists in a solid form with a diffusivity close to 0. In this case, where the product diffuses much more slowly than the reactant, the density profile is also nonmonotonic with a minimum in density [38].

VI. CONCLUSION

We have studied the development of buoyancy-driven convective instabilities generated by CO_2 dissolution in reactive aqueous solutions of calcium ions in a vertical Hele-Shaw cell. Two different reactants were considered to induce a reaction between carbonate and calcium ions dissolved in the aqueous solution, producing solid calcium carbonate: a base $Ca(OH)_2$ and a salt $CaCl_2$. The pH of $CaCl_2$ solutions is too acidic to allow the precipitation of calcium carbonate, so these salt solutions have been buffered to keep the pH of the solutions close to 9 and mimic the natural buffering capacity of geological reservoirs.

In these two configurations, quite different effects were observed. In the case of the dissolution of CO_2 in sufficiently concentrated aqueous solutions of $Ca(OH)_2$, $CaCO_3$ precipitates in solid particles sinking below the reaction front, which intensifies the downward convective motions. On the other hand, precipitation in the presence of $CaCl_2$ has a stabilizing impact on the convective dissolution of CO_2 because of a local decrease in density. The produced solid phase in this case gets attached to the glass substrate. This strongly reduces convective motions in the aqueous phase below the reaction front. In both cases, the presence of a reaction front where the precipitation predominantly takes place is observed to move away from the interface at a steady velocity.

Our results show that the *in situ* formation by a reaction of a solid phase and its settling within convective fingers is a complex system with a moving reaction front separating different zones where the physical properties of the solution are different and change in space and time. It is thus a challenging problem in which convective dissolution, reactions, and settling of particles in convective flows [49,50] are present simultaneously. Here again, we see that a same reaction (i.e., the reaction between calcium and carbonate ions) can induce very different spatiotemporal dynamics depending on the counterions present [45]. More experimental and theoretical works will be needed to unravel all the rich dynamics possibilities of this chemo-hydrodynamic system [51]. In particular, conducting similar analysis of reactive transport in real three-dimensional (3D) porous media would be of special interest [18].

Coming back to CO_2 sequestration, these experimental results could help understanding of the optimal chemical conditions for carbonate mineralization in geological formations as they show that the chemical environment in which the precipitation reaction takes place between carbonate and calcium ions strongly impacts the transport of solid particles in the reservoir. In some cases, weakening by reaction of the convective mixing is observed with precipitation that could result in clogging on the porous matrix. However, in other conditions, the sinking of solid carbonate particles in the flow can enhance convective mixing, which could increase the efficiency and safety of CO_2 storage.

---

[1] J. M. Matter, M. Stute, S. O. Snaebjörnsdottir, E. H. Oelkers, S. R. Gislason, E. S. Aradottir, B. Sigfusson, I. Gunnarsson, H. Sigurdardottir, E. Gunnlaugsson, G. Axelsson, H. A. Alfredsson, D. Wolff-Boenisch, K. Mesfin, D. Fernandez de la Reguera Taya, J. Hall, K. Dideriksen, and W. S. Broecker, Rapid carbon mineralization for permanent disposal of anthropogenic carbon dioxide emissions, Science **352**, 1312 (2016).

[2] B. Metz, O. Davidson, H. C. de Conninck, M. Loos, L. A. Meyer, *IPCC Special Report on Carbon Dioxide Capture and Storage (Working Group III)* (Cambridge University Press, Cambridge, UK, 2005).

[3] H. Emami-Meybodi, H. Hassanzadeh, C. P. Green, and J. Ennis-King, Convective dissolution of CO_2 in saline aquifers: Progress in modeling and experiments, Int. J. Greenh. Gas Control **40**, 238 (2015).

[4] K. Ghesmat, H. Hassanzadeh, and J. Abedi, The impact of geochemistry on convective mixing in a gravitationally unstable diffusive boundary layer in porous media: CO_2 storage in saline aquifers, J. Fluid Mech. **673**, 480 (2011).

[5] J. Ennis-King, I. Preston, and L. Paterson, Onset of convection in anisotropic porous media subject to a rapid change in boundary conditions, Phys. Fluids **17**, 084107 (2005).

[6] J. A. Neufeld, M. A. Hesse, A. Riaz, M. A. Hallworth, H. A. Tchelepi, and H. E. Huppert, Convective dissolution of carbon dioxide in saline aquifers, Geophys. Res. Lett. **37**, L22404 (2010).

[7] C. Thomas, S. Dehaeck, and A. De Wit, Convective dissolution of CO_2 in water and salt solutions, Int. J. Greenh. Gas Control **72**, 105 (2018).

[8] Q. Li, W. Cai, F.-C. Li, B. Li, and C.-Y. Chen, Miscible density-driven flows in heterogeneous porous media: Influences of correlation length and distribution of permeability, Phys. Rev. Fluids **4**, 014502 (2019).

[9] V. Loodts, L. Rongy, and A. De Wit, Impact of pressure, salt concentration, and temperature on the convective dissolution of carbon dioxide in aqueous solutions, Chaos **24**, 043120 (2014).

[10] V. Loodts, C. Thomas, L. Rongy, and A. De Wit, Control of Convective Dissolution by Chemical Reactions: General Classification and Application to CO_2 Dissolution in Reactive Aqueous Solutions, Phys. Rev. Lett. **113**, 114501 (2014).

[11] S. S. S. Cardoso and J. T. H. Andres, Geochemistry of silicate-rich rocks can curtail spreading of carbon dioxide in subsurface aquifers, Nat. Commun. **5**, 5743 (2014).

[12] A. De Wit, Chemo-hydrodynamic patterns in porous media, Philos. Trans. R. Soc. A **374**, 20150419 (2016).

[13] C. A. Rochelle, I. Czernichowski-Lauriol, and A. E. Milodowski, The impact of chemical reactions on CO_2 storage in geological formations: A brief review, Geol. Soc. London Spec. Publ. **233**, 87 (2004).

[14] A. Sanna, M. Uibu, G. Caramanna, R. Kuusik, and M. M. Maroto-Valer, A review of mineral carbonation technologies to sequester CO_2, Chem. Soc. Rev. **43**, 8049 (2014).

[15] G. Schuszter, F. Brau, and A. De Wit, Calcium carbonate mineralization in a confined geometry, Environ. Sci. Techn. Lett. **3**, 156 (2016).

[16] J. J. Hidalgo, M. Dentz, Y. Cabeza, and J. Carrera, Dissolution patterns and mixing dynamics in unstable reactive flow, Geophys. Res. Lett. **42**, 6357 (2015).

[17] P. Szymczak and A. J. C. Ladd, Instabilities in the dissolution of a porous matrix, Geophys. Res. Lett. **38**, L07403 (2011).

[18] R. Moosavi, A. Kumar, A. De Wit, and M. Schröter, Influence of mineralization and injection flow rate on flow patterns in three-dimensional porous media, Phys. Chem. Chem. Phys. **21** 14605 (2019).

[19] L. Luquot and P. Gouze, Experimental determination of porosity and permeability changes induced by injection of CO_2 into carbonate rocks, Chem. Geol. **265**, 148 (2009).

[20] L. Luquot, O. Rodriguez, and P. Gouze, Experimental characterization of porosity structure and transport property changes in limestone undergoing different dissolution regimes, Transp. Porous Media **101**, 507 (2014).

[21] P. Gouze and L. Luquot, X-ray microtomography characterization of porosity, permeability, and reactive surface changes during dissolution, J. Contam. Hydrol. **120–121**, 45 (2011).

[22] G. Davila, L. Luquot, J. M. Soler, and J. Cama, Interaction between a fractured marl caprock and CO_2-rich sulfate solution under supercritical CO_2 conditions, Int. J. Greenh. Gas Control **48**, 105 (2016).

[23] M. M. Smith, Y. Sholokhova, Y. Hao, and S. A. Carroll, Evaporite caprock integrity: An experimental study of reactive mineralogy and pore-scale heterogeneity during brine-CO_2, Exposure. Environ. Sci. Technol. **47**, 262 (2013).

[24] C. Noiriel, B. Madé, and P. Gouze, Impact of coating development on the hydraulic and transport properties in argillaceous limestone fracture, Water Res. Res. **43**, W09406 (2007).

[25] G. Schuszter, F. Brau, and A. De Wit, Flow-driven control of calcium carbonate precipitation patterns in a confined geometry, Phys. Chem. Chem. Phys. **18**, 25592 (2016).

[26] G. Schuszter and A. De Wit, Comparison of flow-controlled calcium and barium carbonate precipitation patterns, J. Chem. Phys. **145**, 224201 (2016).

[27] Y. Nagatsu, Y. Ishii, Y. Tada, and A. De Wit, Hydrodynamic Fingering Instability Induced by a Precipitation Reaction, Phys. Rev. Lett. **113**, 024502 (2014).

[28] I. Gaus, Role and impact of CO_2–rock interactions during CO_2 storage in sedimentary rocks, Int. J. Greenh. Gas Control **4**, 73 (2010).

[29] M. L. Druckenmiller and M. M. Maroto-Valer, Carbon sequestration using brine of adjusted pH to form mineral carbonates, Fuel Proc. Tech. **86**, 1599 (2005).

[30] B. Bohner, G. Schuszter, D. Horvath, and A. Toth, Morphology control by flow-driven self-organizing precipitation, Chem. Phys. Lett. **631–632**, 114 (2015).

[31] G. S. Settles, *Schlieren and Shadowgraph Techniques: Visualizing Phenomena in Transparent Media* (Springer-Verlag, Berlin, 2001).

[32] C. Thomas, L. Lemaigre, A. Zalts, A. D'Onofrio, and A. De Wit, Experimental study of CO_2 convective dissolution: The effect of color indicators, Int. J. Greenh. Gas Control **42**, 525 (2015).

[33] C. Almarcha, P. M. J. Trevelyan, L. A. Riolfo, A. Zalts, C. El Hasi, A. D'Onofrio, and A. De Wit, Active role of a color indicator in buoyancy-driven instabilities of chemical fronts, J. Phys. Chem. Lett. **1**, 752 (2010).

[34] PubChem Compound Database, National Center for Biotechnology Information, https://pubchem.ncbi. nlm.nih.gov/compound/750.

[35] Y. K. Kharaka and J. S. Hanor, Deep fluids in the continents: I. Sedimentary basins, in *Surface and Ground Water, Weathering, and Soils: Treatise on Geochemistry*, edited by J. I. Drever (Elsevier, Amsterdam, 2007), 1–48.

[36] See Supplemental Material at http://link.aps.org/supplemental/10.1103/PhysRevFluids.5.113505 for videos of the dynamics.

[37] C. Almarcha, P. M. J. Trevelyan, P. Grosfils, and A. De Wit, Thermal effects on the diffusive layer convection instability of an exothermic acid-base reaction front, Phys. Rev. E **88**, 033009 (2013).

[38] V. Loodts, P. M. J. Trevelyan, L. Rongy, and A. De Wit, Density profiles around A+B → C reaction-diffusion fronts in partially miscible systems: A general classification, Phys. Rev. E **94**, 043115 (2016).

[39] V. Loodts, B. Knaepen, L. Rongy, and A. De Wit, Enhanced steady-state dissolution flux in reactive convective dissolution, Phys. Chem. Chem. Phys. **19**, 18565 (2017).

[40] V. Loodts, H. Saghou, B. Knaepen, L. Rongy, and A. De Wit, Differential diffusivity effects in reactive convective dissolution, Fluids **3**, 83 (2018).

[41] M. Jotkar, L. Rongy, and A. De Wit, Reactive convective dissolution with differential diffusivities: Nonlinear simulations of onset times and asymptotic fluxes fluids, Phys. Rev. Fluids **5**, 104502 (2020).

[42] J. Carballido-Landeira, P. M. J. Trevelyan, C. Almarcha, and A. De Wit, Mixed-mode instability of a miscible interface due to coupling between Rayleigh-Taylor and double-diffusive convective modes, Phys. Fluids **25**, 024107 (2013).

[43] R. E. Zeebe and D. Wolf-Gladrow, CO_2 *in Seawater: Equilibrium, Kinetics, Isotopes* (Elsevier, Amsterdam, 2001).

[44] W. M. Haynes, *CRC Handbook of Chemistry and Physics 2016–2017*, 97th ed. (CRC Press, Boca Raton, FL, 2016).

[45] C. Thomas, V. Loodts, L. Rongy, and A. De Wit, Convective dissolution of CO_2 in reactive alkaline solutions: Active role of spectator ions, Int. J. Greenh. Gas Control **53**, 230 (2016).

[46] M. C. Kim and S. S. S. Cardoso, Diffusivity ratio effect on the onset of the buoyancy-driven instability of an A + B → C chemical reaction system in a Hele-Shaw cell: Asymptotic and linear stability analyses, Phys. Fluids **30**, 094102 (2018).

[47] C. Wylock, S. Dehaeck, A. Rednikov, and P. Colinet, Chemo-hydrodynamical instability created by CO_2 absorption in an aqueous solution of $NaHCO_3$ and Na_2CO_3, Microgravity Sci. Technol. **20**, 171 (2008).

[48] C. Almarcha, P. M. J. Trevelyan, P. Grosfils, and A. De Wit, Chemically Driven Hydrodynamic Instabilities, Phys. Rev. Lett. **104**, 044501 (2010).

[49] C. Völtz, W. Pesch, and I. Rehberg, Rayleigh-Taylor instability in a sedimenting suspension, Phys. Rev. E **65**, 011404 (2001).

[50] S. Harada, M. Kondo, K. Watanabe, T. Shiotani, and K. Sato, Collective settling of fine particles in a narrow channel with arbitrary cross-section, Chem. Eng. Sci. **93**, 307 (2013).

[51] A. De Wit, Chemo-hydrodynamic patterns and instabilities, Annu. Rev. Fluid Mech. **52**, 531 (2020).